CrossMark

# Changes in ENSO amplitude under climate warming and cooling

Yingying Wang[1] · Yiyong Luo[1] · Jian Lu[2] · Fukai Liu[1]

## Abstract

The response of ENSO amplitude to climate warming and cooling is investigated using the Community Earth System Model (CESM), in which the warming and cooling scenarios are designed by adding heat fluxes of equal amplitude but opposite sign onto the ocean surface, respectively. Results show that the warming induces an increase of the ENSO amplitude but the cooling gives rise to a decrease of the ENSO amplitude, and these changes are robust in statistics. A mixed layer heat budget analysis finds that the increasing (decreasing) SST tendency under climate warming (cooling) is mainly due to an enhancement (weakening) of dynamical feedback processes over the equatorial Pacific, including zonal advective (ZA) feedback, meridional advective (MA) feedback, thermocline (TH) feedback, and Ekman (EK) feedback. As the climate warms, a wind anomaly of the same magnitude across the equatorial Pacific can induce a stronger zonal current change in the east (i.e., a stronger ZA feedback), which in turn produces a greater weakening of upwelling (i.e., a stronger EK feedback) and thus a larger thermocline change (i.e., a stronger TH feedback). In response to the climate warming, in addition, the MA feedback is also strengthened due to an enhancement of the meridional SST gradient around the equator resulting from a weakening of the subtropical cells (STCs). It should be noted that the weakened STCs itself has a negative contribution to the change of the MA feedback which, however, appears to be secondary. And vice versa for the cooling case. Bjerknes linear stability (BJ) index is also evaluated for the linear stability of ENSO, with remarkably larger (smaller) BJ index found for the warming (cooling) case.

**Keywords** ENSO amplitude · Climate warming · Climate cooling · Dynamical feedbacks · BJ index

## 1 Introduction

The El Niño-Southern Oscillation (ENSO) cycle of alternating warm El Niño and cold La Niña events dominates the interannual climate variability in the Pacific (e.g., Philander 1990; McPhaden et al. 2006). It originates in the tropical Pacific through ocean and atmosphere interactions and has a vital important role on influencing the global climate via teleconnections (Horel and Wallace 1981). ENSO is sensitive to changes in global temperatures (Tsonis et al. 2003) and is the important source of predictability (Zheng et al. 2016).

While scientists devote to improving ENSO simulation, extensive studies have also explored the changes in characteristics of ENSO under different climate scenarios. By analyzing simulations from the Climate Model Intercomparison Project versions 3 (CMIP3) and 5 (CMIP5), for instance, it has been found that the frequencies of extreme El Niño, extreme La Niña and ENSO-related catastrophic weather events are likely to be increasing in the future in response to greenhouse gases (GHG)-induced warming (Cai et al. 2014, 2015). Analyses of CMIP3 (Merryfield 2006) also suggested a fractional decrease in ENSO period of about 5% under $CO_2$ doubling in a multi-model ensemble. In addition, the ENSO teleconnection pattern in the Pacific–North America sector has also been shown to shift eastward in a warmer climate relative to the present-day climate (Bulić et al. 2012; Zhou et al. 2014).

In terms of the response of the ENSO amplitude itself to global warming, however, there is a large diversity among climate models (e.g., Van Oldenborgh et al. 2005; Philip and Van Oldenborgh 2006; Capotondi et al. 2006; Kim

✉ Yiyong Luo
  yiyongluo@ouc.edu.cn

1  Physical Oceanography Laboratory/CIMST, Ocean University of China, Qingdao National Laboratory for Marine Science and Technology, 238 Songling Road, Qingdao 266100, China

2  Atmospheric Sciences and Global Change Division, Pacific Northwest National Laboratory, Richland, WA, USA

and Jin 2011; Bellenger et al. 2014; Kim et al. 2014; Chen et al. 2015, 2017; Zheng et al. 2016). The ENSO amplitude change based on the multi-model mean from CMIP5 is indistinguishable from zero (Stevenson 2013). The diversity of ENSO amplitudes among different models makes it impossible to obtain definite conclusions about how the SST amplitude changes in the future (Watanabe et al. 2012; Bellenger et al. 2014), but it is important to explore what physical mechanisms affect the variances when the mean state changes. Yeh and Kirtman (2007) studied the regime behavior of ENSO and its link to the ENSO amplitude and suggested that the model lying in the nonlinear ENSO regime is more sensitive to the mean state changes due to $CO_2$ forcing. By examining two ENSO-strengthened models and two ENSO-weakened models in CMIP5 and focusing on the key processes related to ENSO dynamics, Chen at al. (2015) argued that the diversity in ENSO amplitude is primarily attributed to distinctive basic-state SST and wind stress changes in the tropical Pacific which, through a so-called indirect effect, influences the perturbation structure and air–sea feedback strength. Further, they extended their examination to a larger collection of models in CMIP5 (Chen et al. 2017) and found that the strength of the subtropical cells (STC) determines the meridional structure of ENSO perturbations and thus the anomalous thermocline response to the wind forcing. Through a comparison of the historical climate experiments with the 8.5 W m$^{-2}$ Representative Concentration Pathway (RCP8.5) experiments in CMIP5, Zheng et al. (2016) suggested that the mean SST warming pattern plays a dominant role on the ENSO amplitude response to global warming. In addition, Kim and Jin (2011) found a significant positive correlation between ENSO amplitude and ENSO stability as measured by the Bjerknes linear stability (BJ) index in the twentieth and twenty-first century simulations in CMIP3. However, their further study (Kim et al. 2014) showed that this linear relationship does not work for some of the models in CMIP5 due to different level of nonlinearity and noise in them.

In contrast to what happens under GHG forcing, recent studies found that aerosol forcing induces a similar pattern of response but opposite in sign (Xie et al. 2013). For example, over the tropical Indian Ocean, while the GHG induces a positive Indian Ocean dipole-like response, the mean climate condition shifts toward a negative Indian Ocean dipole-like state under aerosol forcing (Dong et al. 2014; Cowan et al. 2015). Further, the changes are asymmetric, with the aerosol effect exceeding the GHG effect (Li and Luo 2018). Through a set of experiments with the National Center for Atmospheric Research (NCAR) Community Earth System Model (CESM), we recently examined the response of the mean states in the equatorial Pacific to climate warming and cooling. It was found that there appear asymmetric changes in many of surface and subsurface fields over the equatorial Pacific Ocean

(Liu et al. 2017a). By examining the ENSO amplitude changes under climate warming and cooling, our focus in this study is to understand the mechanisms behind these changes. The main reason for choosing the NCAR's CESM is that the model exhibits good skills in representing ENSO characteristics in the present-day simulation and it is actually one of the best models in CMIP5 in simulating basic ENSO features and ENSO-related air-sea feedbacks (e.g., Bellenger et al. 2014; Liu et al. 2017b). The rest of the paper is structured as follows. Section 2 briefly introduces the experiments with CESM. Section 3 compares the ENSO amplitude changes between climate warming and cooling. Through a mixed layer heat budget analysis, Sect. 4 examines the dominant dynamic and thermodynamic feedbacks to understand the processes responsible for the ENSO amplitude changes. In Sect. 5, the BJ index as an overall measurement of the relative contributions of positive feedback effect and damping process effect is calculated and discussed. Section 6 concludes with a summary of the main findings.

## 2 Experiments with CESM

The CESM used for this study consists of the Community Atmospheric Model version 5 (CAM5), the Community Land Model version 4 (CLM4) and the Parallel Ocean Program version 2 (POP2). The control simulation is integrated for 250 years with no external forcing in the coupled atmosphere–ocean system. In parallel, the heating and cooling simulations are also integrated for 250 years by adding a uniform heat flux of 6 and $-6$ W m$^{-2}$ into the ocean surface, respectively. These heat fluxes are added into the surface ocean every step the atmosphere and ocean communicate through the coupler. We refer to the three simulations as the reference climate simulation (RFS), climate warming simulation (WMS), and climate cooling simulation (CLS), respectively. Results presented below are from the last 100 years of the model integration when the upper ocean reaches a quasi-equilibrium stage (Liu et al. 2017a), and the responses to the heating and cooling forcing are taken as WMS–RFS and CLS–RFS, respectively. A note is that all time series of the raw data from 250 years are first detrended and monthly anomalies are then obtained by further removing the model climatological annual cycle from the last 100 years of the detrended data. In addition, a 1400-year control simulation with the same setting as for the RFS is obtained from NCAR in order to examine the statistical significance of ENSO amplitude variations.

## 3 Changes in ENSO amplitude under climate warming and cooling

Figure 1 compares the interannual standard deviation (STD) of SST anomaly (SSTA) among RFS (Fig. 1a), WMS (Fig. 1b), and CLS (Fig. 1c). Under climate warming, the SSTA STD shows an overall increase in the equatorial Pacific, with a large enhancement in the eastern basin and weak reduction around the dateline; under climate cooling, the equatorial peak of the STD weakens coherently across the whole equatorial Pacific. In this study, the ENSO amplitude is defined as the SSTA STD over the Niño3 region (150°W–90°W, 5°N–5°S), in which the variance appears to be large for all three cases. Figure 2 shows the SSTA STD in WMS (the red dot; 1.52 K) and CLS (the blue dot; 0.69 K) relative to the probability density function of Niño3 mean SSTA STD in a 1400-year control simulation, indicating that the ENSO amplitude changes in both WMS and CLS are statistically robust.

To assess the changes of ENSO amplitude quantitatively, we construct an El Niño (La Niña) composite based on the last 100 years of simulations in RFS, WMS and CLS, respectively. It's known that the peak of El Niño (La Niña) events usually occur in November, December and the following
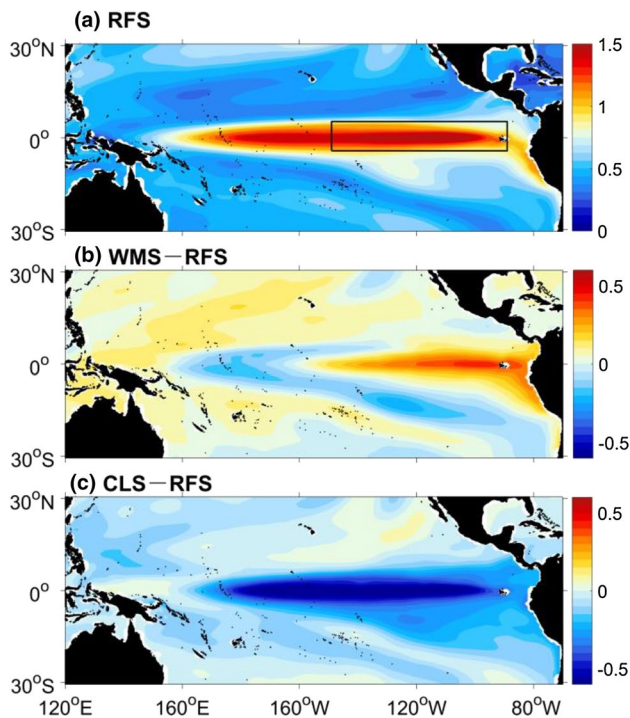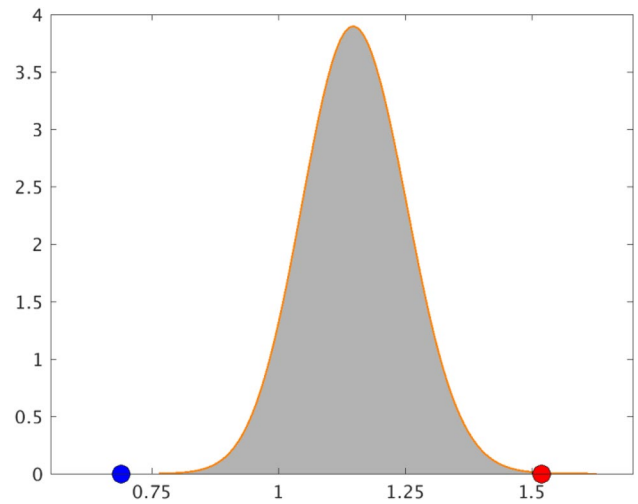


**Fig. 2** The probability density function (PDF) of SSTA STD in the Niño3 region and the STD in WMS (red dot), and CLS (blue dot). The PDF is calculated with 1000 samples, with each sample being created by randomly selecting 200-year data from the 1400-year control run. Note that the PDF is smoothed with a Gaussian window

January. The criterion for selecting events is that the SSTA over the Niño3 region during November$^0$, December$^0$ and January$^{+1}$ exceeds one STD in the corresponding climate state. Figure 3 shows the composite results of El Niño and La Niña events in RFS, WMS and CLS, respectively. It shows that the peak SSTA of ENSO changes significantly, with an increase of 0.67 K or 18% from 3.67 K in RFS to 4.34 K in WMS and a decrease of 1.34 K or 36% to 2.33 K in CLS. If we define the 8 months from April$^0$ to November$^0$ as the developing phase, the growth rate of ENSO amplitude increases by 0.24 K month$^{-1}$ in WMS and decreases by 0.21 K month$^{-1}$ in CLS compared to 0.43 K month$^{-1}$



**Fig. 1** Interannual standard deviation (STD; K) of sea surface temperature anomaly (SSTA) in **a** RFS, and its changes in **b** WMS, and **c** CLS. The black box in **a** indicates the Nino3 region (150°W–90°W, 5°N–5°S)
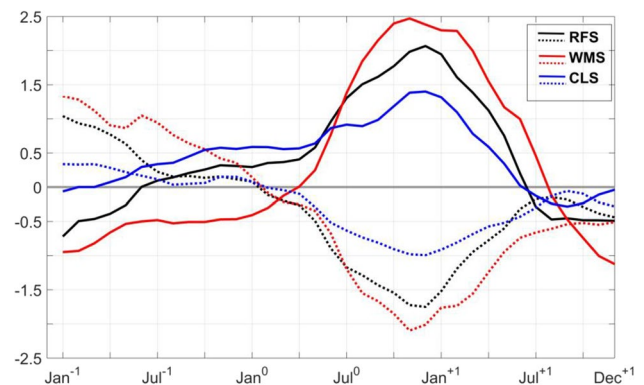


**Fig. 3** The composite SSTA (K) in the Niño3 region during El Niño (solid) and La Niña (dashed) periods in RFS (black), WMS (red), and CLS (blue). Superscripts −1,0 and +1 in Jan, Jul and Dec denote the 3 years before and after El Niño/La Niña events. The gray line is zero reference line

in RFS. Therefore, the response of the ENSO amplitude to climate warming and cooling appears a sharp contrast.

## 4 Dominant dynamic and thermodynamic processes for ENSO amplitude changes

### 4.1 Mixed layer heat budget analysis

To explore the mechanisms for the changes in ENSO amplitude under climate warming and cooling, we perform a heat budget analysis by employing the thermodynamic equation (Philander 1990) for the Niño3 region:

$$\frac{\partial T'}{\partial t} = -(\mathbf{V}' \cdot \nabla \bar{T} + \bar{\mathbf{V}} \cdot \nabla T')) - (\mathbf{V}' \cdot \nabla T') + \frac{Q'_{net}}{\rho_0 C_p H} + \delta \tag{1}$$

where $T$ is the mixed layer temperature, $\mathbf{V}$ represents three-dimensional ocean current vector, $Q_{net}$ is the net download heat flux, $\rho_0$ is the density of seawater, $C_p$ is the specific heat of water, $H = 55$ m is the mixed layer depth. A note that it has been a common practice to use an upper layer with a flat bottom to diagnose the SST evolution (e.g., DiNezio et al. 2009, 2012; Alory and Meyers 2009), and the 0–55 m layer temperature has very similar interannual variability to the SST in our experiments. $\delta$ denotes the residual term that represents the ocean heat transport by unresolved sub-grid scale processes as well as sub-monthly oceanic processes, and $\nabla = (\partial/\partial x, \partial/\partial y, \partial/\partial z)$ is the three-dimensional gradient operator.

The mixed layer heat budget analysis is applied to diagnose the tendency of mixed layer temperature anomaly (MLTA) during the developing phase of the composite El Niño and La Niña events. In our calculation, each budget term is first obtained for compositing El Niño and La Niña events over the Niño3 region, and then taking the difference between El Niño and La Niña (El Niño minus La Niña). Changes in the mixed layer heat budget terms are shown in Fig. 4a from RFS to WMS and in Fig. 4b from RFS to CLS, respectively.

It is found that the tendency of MLTA is increased by 0.23 K month$^{-1}$ from RFS to WMS (bar 12 in Fig. 4a) but is decreased by 0.19 K month$^{-1}$ from RFS to CLS (bar 12 in Fig. 4b). Based on the first 10 terms on the right side of Eq. (1), the estimated MLTA tendency (bar11 in Fig. 4) is very close to the actual MLTA tendency (bar 12 in Fig. 4), indicating that the mixed layer heat budget diagnostic results are credible. Their differences could be due to unresolved ocean diffusion processes and computational errors.

To identify the major terms responsible for the ENSO amplitude changes under climate warming and cooling, the differences of mixed layer heat budget terms in the Nino3 region between WMS and CLS are summarized
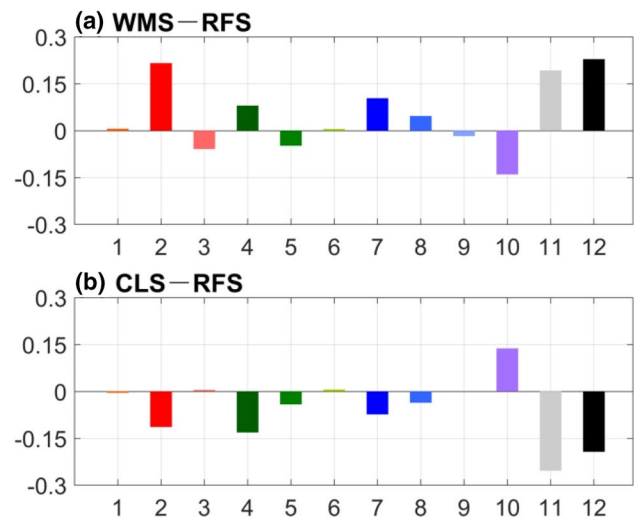


**Fig. 4** Changes in the mixed layer heat budgets over the Niño3 region in which each budget term (K month$^{-1}$) is first obtained for El Niño and La Niña composite (El Niño minus La Niña): **a** from RFS to WMS, and **b** from RFS to CLS. Bars 1–9 represent the changes in the zonal, meridional, and vertical advection terms, bar 10 is the change in the net surface heat flux term, and bar 11 is the sum of the above 10 terms. Bar 12 denotes the change in the mixed layer temperature anomaly tendency. The expressions of these bars are as follows: $d(-\bar{u} \cdot \partial T'/\partial x)$ (bar1), $d(-u' \cdot \partial \bar{T}/\partial x)$ (bar2), $d(-u' \cdot \partial T'/\partial x)$ (bar3), $d(-\bar{v} \cdot \partial T'/\partial y)$ (bar4), $d(-v' \cdot \partial \bar{T}/\partial y)$ (bar5), $d(-v' \cdot \partial T'/\partial y)$ (bar6), $d(-\bar{w} \cdot \partial T'/\partial z)$ (bar7), $d(-w' \cdot \partial \bar{T}/\partial z)$ (bar8), $d(-w' \cdot \partial T'/\partial z)$ (bar9), $d(Q_{net}/\rho_0 C_p H)$ (bar10), and $d(\partial T'/\partial t)$ (bar12)

in Table 1. We find that the air-sea surface heat flux term 10 ($Q_{net}/\rho_0 C_p H$) is the major damping term to the ENSO amplitude changes in both WMS and CLS. This term is referred to as the thermodynamic damping (TD) feedback and will be discussed in Sect. 4.6. Since the change of the surface heat flux acts as a damping role, the evolution of difference in ENSO amplitude must be driven by the ocean dynamics. Thus, for the first, our analysis will focus on the changes of dynamical feedback processes.

It can be seen from Table 1 that terms 2, 4, 7, and 8 are the four major ones that play a positive role for increasing (decreasing) MLTA in WMS (CLS). They represent the advection of mean temperature by anomalous zonal current ($-u' \cdot \partial \bar{T}/\partial x$), the advection of anomalous temperature by mean meridional current ($-\bar{v} \cdot \partial T'/\partial y$), the advection of anomalous temperature by mean vertical velocity ($-\bar{w} \cdot \partial T'/\partial z$), and the Ekman pumping induced anomalous upwelling feedback ($-w' \cdot \partial \bar{T}/\partial z$), respectively. Following Chen et al. (2015, 2017), in this study we call term 2 the zonal advective (ZA) feedback, term 4 the meridional advective (MA) feedback, term 7 the thermocline (TH) feedback, and term 8 the Ekman (EK) feedback. In addition, these four major terms are all linear dynamic terms, while the nonlinear dynamic terms make less contribution (terms 3, 6 and 9 in Table 1).

**Table 1** Differences of mixed layer heat budget terms (K month$^{-1}$) in the Nino3 region (150°W–90°W, 5°N–5°S) between WMS and CLS

| Term 1 | Term 2 | Term 3 | Term 4 | Term 5 | Term 6 | Term 7 | Term 8 | Term 9 | Term 10 |
|---|---|---|---|---|---|---|---|---|---|
| $d\left(-\bar{u}\frac{\partial T'}{\partial x}\right)$ | $d\left(-u'\frac{\partial \bar{T}}{\partial x}\right)$ | $d\left(-u'\frac{\partial T'}{\partial x}\right)$ | $d\left(-\bar{v}\frac{\partial T'}{\partial y}\right)$ | $d\left(-v'\frac{\partial \bar{T}}{\partial y}\right)$ | $d\left(-v'\frac{\partial T'}{\partial y}\right)$ | $d\left(-\bar{w}\frac{\partial T'}{\partial z}\right)$ | $d\left(-w'\frac{\partial \bar{T}}{\partial z}\right)$ | $d\left(-w'\frac{\partial T'}{\partial z}\right)$ | $d\left(\frac{Q_{net}}{\rho_0 C_p H}\right)$ |
| 0.01 | 0.33 | −0.06 | 0.22 | −0.01 | 0.00 | 0.17 | 0.09 | −0.02 | −0.28 |

The first nine terms represent the changes in the zonal, meridional, and vertical advections, and term 10 denotes the change in the net surface heat flux. Highlighted by bold are the five major terms that will be analyzed in this study
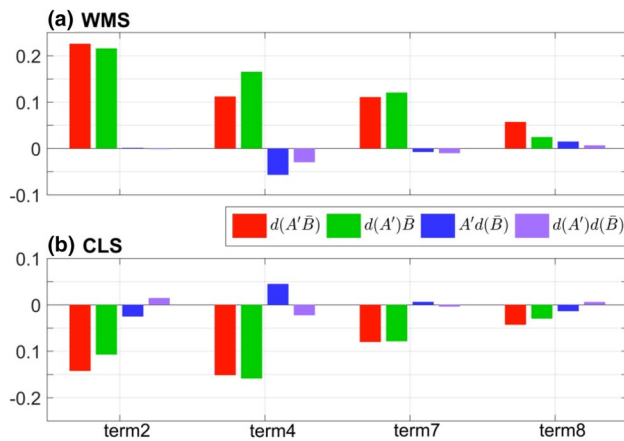


**Fig. 5** Relative contributions of mean state change and perturbation change to variations in the budget terms of zonal advective (ZA) feedback [term2, $d(-u' \cdot \partial \bar{T}/\partial x)$], meridional advective (MA) feedback [term4, $d(-\bar{v} \cdot \partial T'/\partial y)$], thermocline (TH) feedback [term7, $d(-\bar{w} \cdot \partial T'/\partial z)$], and Ekman (EK) feedback [term8, $d(-w' \cdot \partial \bar{T}/\partial z)$] for **a** WMS, and **b** CLS



**Fig. 6** Regression coefficient changes (color; m s$^{-1}$ (N m$^{-2}$)$^{-1}$) of the zonal current anomaly ($u'$) regressed onto the zonal wind anomaly ($\tau'_x$) over the equatorial Pacific (120°E–80°W, 5°N–5°S): **a** from RFS to WMS, and **b** from RFS to CLS. Contours in the two panels are the corresponding vertical velocity changes ($w'$) [contour interval (CI) = $0.25 \times 10^{-6}$ m s$^{-1}$] during the ENSO developing phase, with negative by black, positive by red, and zero by white

Since all these four terms discussed above are product of the mean and anomalous states, both of which changes remarkably in response to the warming and cooling, we examine to what extent the mean state change and the perturbation change contribute to changes in these heat budget terms. Following Chen et al. (2015, 2017), we separate their relative contributions based on the following total differential relationship:

$$d(A'\bar{B}) = d(A')\bar{B} + A'd(\bar{B}) + d(A')d(\bar{B}) \qquad (2)$$

where operator $d(\cdot)$ denotes the difference from RFS to WMS or CLS, $A'$ represents the perturbation, and $\bar{B}$ represents the mean state. According to Eq. (2), the change of product of $A'$ and $\bar{B}$ can be decomposed into the perturbation contribution $d(A')\bar{B}$, the mean state contribution $A'd(\bar{B})$, and the residual $d(A')d(\bar{B})$ related to covariance between the mean state and perturbation changes.

Figure 5 shows that, for all the four terms, it is the change of perturbation rather than the mean state that plays a major role for the SSTA tendency change. In other words, these changes of the four major budget terms are all resulted mainly 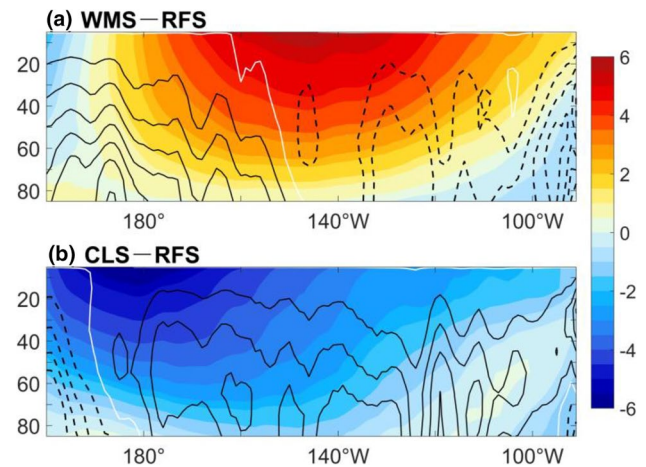from the perturbation changes, while the contributions from the mean state changes are minor. Therefore, in the following discussions we will examine the contributions from the perturbation changes to the changes of the terms in the order of importance.

## 4.2 Zonal advective feedback

As described above, the change of anomalous zonal current makes a major contribution to the ZA feedback. We regress the zonal ocean current anomaly field ($u'$) along the equator onto $\tau'_x$ across the equatorial Pacific (120°E–80°W, 5°N–5°S) in RFS, WMS, and CLS, respectively. The zonal-vertical distributions of their coefficients indicate that a westerly wind anomaly over the equatorial ocean is accompanied by eastward anomalous zonal currents over the central and eastern equator in all three cases (not shown). The regression coefficients are increased from RFS to WMS but decreased from RFS to CLS (Fig. 6), with the most significant changes being over the eastern equator for the former but over the central equator for the latter. Under climate

warming, the increased regression coefficients suggest a stronger response of anomalous zonal currents to the zonal wind stress anomaly, i.e., the ZA feedback is strengthened so the wind anomaly in the equatorial Pacific can induce a larger zonal current anomaly and higher SST in the eastern Pacific. In addition, previous studies have identified the enhanced zonal wind anomaly response to ENSO-related SSTA under global warming from CMIP5 multi-model ensemble (e.g., Li et al. 2016, 2017), which is also favorable to the strengthened ZA feedback. Under climate cooling, on the contrary, the decreased regression coefficients indicate a weaker response of anomalous zonal currents to the zonal wind anomaly, i.e., the ZA feedback is weakened so the same wind anomaly will produce a smaller zonal current anomaly and lower SST in the eastern Pacific. Such changes in the ZA feedback favor the ENSO amplitude changes in both WMS and CLS.

To further explore the nature of the zonal current response, the anomalous zonal geostrophic and Ekman currents along the equator are obtained based upon the following equations (e.g., Su et al. 2010):

$$u'_g = -\frac{g'\partial^2 D'}{\beta \partial y^2} \tag{3}$$

$$u'_E = -\frac{1}{\rho_0 H}\frac{r_s \tau'_x + \beta y \tau'_y}{r_s^2 + (\beta y)^2} \tag{4}$$

where $g'$ is the reduced gravity ($g' = 0.026$ m s$^{-1}$), $D'$ represents the thermocline depth anomaly, $y$ is the latitude, $\beta = 2.28 \times 10^{-11}$ m$^{-1}$ s$^{-1}$ is the planetary vorticity gradient, $\tau'_x$ and $\tau'_y$ are the zonal and meridional wind stress anomalies, and $r_s = 0.5$ day$^{-1}$ is the dissipation rate.

Figure 7 illustrates the anomalous zonal currents, anomalous geostrophic currents and anomalous Ekman currents over the eastern equator for three cases. It is clear that the change of anomalous zonal currents ($u'$) is dominated by geostrophic current ($u'_g$), which appears to be one order of magnitude larger than Ekman current ($u'_E$), indicating that it is actually zonal geostrophic current anomaly that plays the dominant role for the change in the ZA feedback. According to Eq. (3), further, the zonal geostrophic current response is due to a change of the thermocline pattern.

## 4.3 Meridional advective feedback

To explore the response of mean meridional circulation, Fig. 8 shows changes in the meridional currents averaged over the central and eastern equatorial Pacific under climate warming and cooling. It is found that the divergent flows of near-surface water are weakened in WMS but strengthened in CLS. Meanwhile, there is a change in
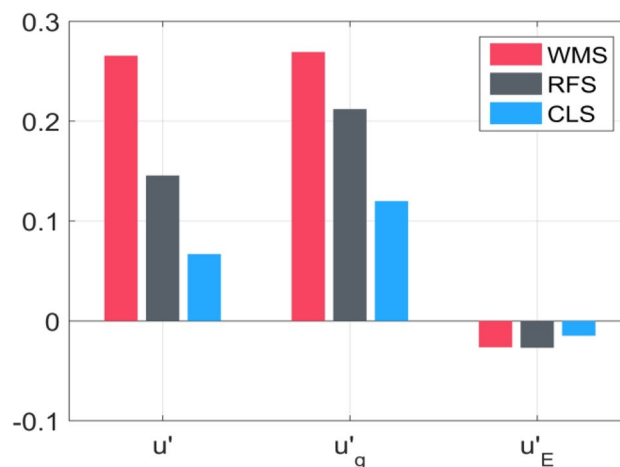


**Fig. 7** The anomalous zonal currents ($u'$; m s$^{-1}$), anomalous geostrophic currents ($u'_g$; m s$^{-1}$), and anomalous Ekman currents ($u'_E$; m s$^{-1}$) over the eastern equator in WMS (red bars), RFS (dark grey bars), and CLS (blue bars) during the developing phase of ENSO. These anomalous currents are obtained by averaging over 2°S–2°N, 120°W–80°W, and 0–30 m



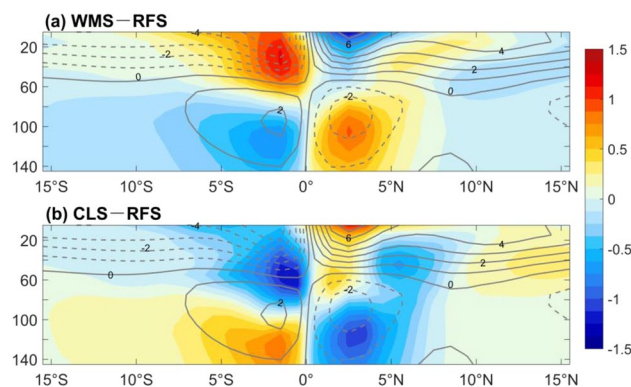**Fig. 8** Changes in the meridional currents (color; cm s$^{-1}$) averaged over 160°E–90°W: **a** from RFS to WMS, and **b** from RFS to CLS. Superimposed are the climatological meridional currents in RFS (CI = 1 cm s$^{-1}$)

the subsurface equatorward flows, with a weakening in WMS and an intensifying in CLS. Following McPhaden and Zhang (2002), we use the water volume transport for the equatorial strip between 9°N and 9°S across the entire Pacific Ocean to represent the STC strength. It is found that the surface layer divergence (i.e., the upper branch of the STC) is reduced by 2.4 Sv from 46.6 Sv in RFS to 44.2 Sv in WMS but is enhanced by 3.0–49.6 Sv in CLS (Table 2). A detailed calculation of meridional volume transport is given in "Appendix A". Both Ekman transport and surface layer geostrophic transport contribute to these changes in WMS and CLS. Correspondingly, the mean pycnocline convergence (i.e., the lower branch of the STC)

**Table 2** Climatological surface layer divergence and interior pycnocline convergence between 9°N and 9°S across the Pacific Ocean in RFS, WMS, and CLS

|  | RFS | WMS | CLS |
|---|---|---|---|
| Surface layer divergence (Sv) | 46.6 | 44.2 | 49.6 |
| Ekman transport (Sv) | 60.1 | 56.3 | 64.2 |
| Surface layer geostrophic transport (Sv) | 13.6 | 12.1 | 14.7 |
| Interior ocean pycnocline convergence (Sv) | 10.0 | 5.8 | 13.8 |

Surface layer divergence is obtained by Ekman transport minus the opposing surface layer geostrophic transport

appears to be decreased in WMS but increased in CLS (Table 2). The decreased tendency of the STC transport under climate warming is in agreement with climate model projections (e.g., Chen et al. 2017).

As shown in Fig. 5, although the above change in the meridional current has a negative impact on the MA feedback, it contributes positively to the meridional scale of SSTA in the eastern equator (Zhang et al. 2013), which dominates the change of the MA feedback. In other words, a weaker meridional current is favorable for a narrower meridional width of ENSO SSTA and thus a stronger MA feedback through its effect on the meridional SST gradient. To examine the response of the meridional scale of SSTA to climate warming and cooling, here we follow Merryfield (2006) and calculate the width index (WI) of SSTA by $WI(SSTA) = \int SSTA|y|dy / \int SSTA \cdot dy$, where y is the latitude and the range of integration is from 5°S to 5°N. It is found that the meridional scales of SSTA is decreased from 2.65 in RFS to 2.57 in WMS but increased to 2.69 in CLS. Therefore, the narrower (wider) meridional width of SSTA in WMS (CLS) induces a larger (smaller) meridional gradient of anomalous temperature, leading to a larger (smaller) MA feedback in WMS (CLS).
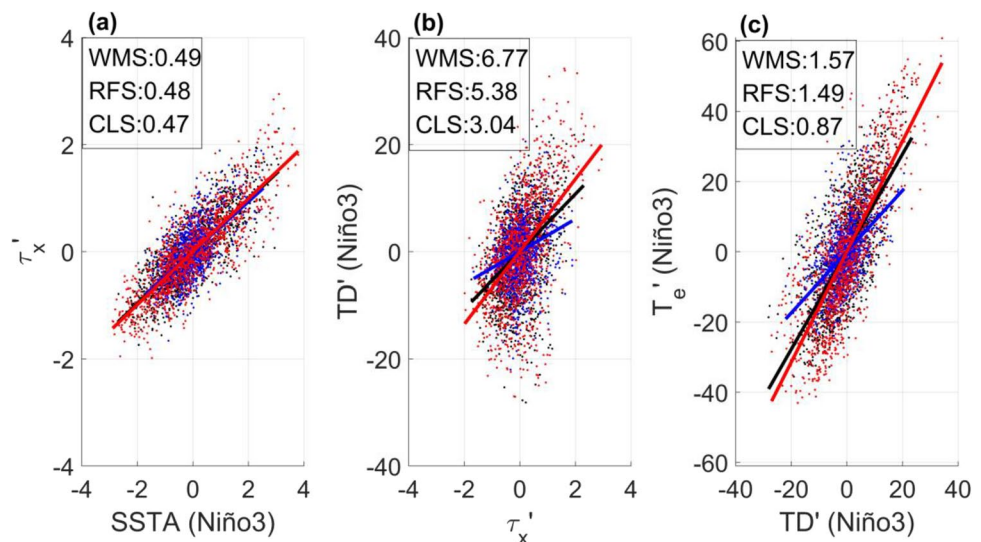
## 4.4 Thermocline feedback

Following Liu et al (2011) and Chen et al (2015), the strength of the TH feedback can be measured by the growth rate:

$$\sigma = \frac{\bar{w}}{H} R(\tau_x', T') R(TD', \tau_x') R(T_e', TD') \qquad (5)$$

where $\bar{w}$ represents the mean vertical velocity, $H$ the mean mixed layer depth, $\tau_x'$ zonal wind stress anomaly, $TD'$ the thermocline depth anomaly, $T'$ the SSTA, and $T_e'$ the oceanic temperature anomaly at subsurface. Equation (5) suggests that, in addition to the climatological upwelling velocity, the ENSO growth rate related to the TH feedback is determined by three feedback coefficients: $R(\tau_x', T')$ represents how the $\tau_x'$ across the equatorial Pacific would change in response to the SSTA over the eastern equator, $R(TD', \tau_x')$ is the effect of a unit zonal wind stress on the change of thermocline over the eastern equator, and $R(T_e', TD')$ represents how the oceanic subsurface temperature would change in response to a unit $TD'$ over the eastern equatorial Pacific.

Since the change in the mean upwelling has a minor contribution to the TH feedback (Fig. 5), we focus on the abovementioned three coefficients. Figure 9 shows the scatters plots and fitted relationships of the SSTA in Niño3 and zonal wind stress anomaly across the equatorial Pacific, the thermocline depth anomaly in Niño3 and zonal wind stress anomaly, and the thermocline depth anomaly in Niño3 and the subsurface temperature anomaly in Niño3 during developing phases in RFS, WMS and CLS, respectively. These fitted linear relationships are used to estimate the strengths of $R(\tau_x', T')$, $R(TD', \tau_x')$, and $R(T_e', TD')$, respectively. It can be seen that, while the SST-wind stress coupling coefficient is largely unchanged (Fig. 9a), the major contrast comes from the thermocline



**Fig. 9** The scatters plots and fitted relationships: **a** between Niño3 SSTA (K) and zonal wind stress anomaly $\tau_x'$ ($10^{-2}$ N m$^{-2}$) over the equatorial Pacific (120°E–80°W, 5°N–5°S), **b** between $\tau_x'$ ($10^{-2}$ N m$^{-2}$) and Niño3 thermocline depth anomaly $TD'$ (m), and **c** between Niño3 $TD'$ (m) and Niño3 subsurface temperature anomaly $T_e'$ (10 K) in RFS (black points and lines), WMS (red points and lines), and CLS (blue points and lines). The corresponding regression slopes are shown at the upper left corner of each panel. The temperature anomalies at the depth of 80 m are used to obtain $T_e'$

response to the zonal wind stress forcing (Fig. 9b) and the subsurface temperature response to the thermocline depth (Fig. 9c). As the climate warms, both $R(TD', \tau'_x)$ and $R(T'_e, TD')$ are increased, leading to a stronger growth rate and thus an enhanced TH feedback. As the climate cools, on the contrary, these two coupling coefficients are decreased, resulting in a weaker growth rate and thus a weakened TH feedback. In addition, it appears that the change in $R(TD', \tau'_x)$ (i.e., the thermocline and zonal wind interaction process) takes the leading role for the change of the TH feedback.

A further analysis finds that these above changes of $R(TD', \tau'_x)$ and $R(T'_e, TD')$ are related to the mean state changes. For $R(TD', \tau'_x)$, we calculate the meridional width of zonal wind anomaly ($\tau'_x$) between 5°S and 5°N based on regressions onto $\tau'_x$ in Niño4 averaged over 160°E-90°W. It is found that the meridional width of $\tau'_x$ becomes narrower from 2.73 in RFS to 2.71 in WMS and wider from 2.73 in RFS to 2.84 in CLS. Based upon previous studies (e.g., Chen et al. 2015, 2017), a change in the meridional structure of $\tau'_x$ would induce a change in the thermocline response to $\tau'_x$. Specifically, a narrower (wider) meridional gradient of $\tau'_x$ induces a greater (smaller) thermocline response, leading to a larger (smaller) $R(TD', \tau'_x)$ in WMS (CLS). While for $R(T'_e, TD')$, we calculate the vertical distribution and gradient of mean temperature over the eastern box (5°S–5°N, 150°W–90°W) in RFS, WMS and CLS (not shown). It is found that the upper ocean is more stratified in WMS but less stratified in CLS. This indicates that, given the same unit change of thermocline depth anomaly, the ocean subsurface temperature would change more (less) and thus result in a larger (smaller) $R(T'_e, TD')$ in WMS (CLS) (e.g., Chen et al. 2016).

## 4.5 Ekman feedback

As demonstrated in Fig. 5, the change of the anomalous upwelling plays a dominant role for the EK feedback. Under climate warming, the stronger response of the zonal currents to the zonal wind anomaly strengthens the surface water convergence during the development of ENSO and thus inhibits the upwelling in the eastern Pacific (contours in Fig. 6a), resulting in an intensification of the EK feedback. Under climate cooling, it is the other way around and the upwelling is enhanced over the eastern Pacific (contours in Fig. 6b) and the EK feedback is thus weakened.

## 4.6 Thermodynamic damping

The mixed layer heat budget analysis finds that the change in the TD term is the major damping factor for the ENSO amplitude changes in both WMS and CLS (Fig. 4). Changes in the total surface heat flux as well as its three components are shown in Fig. 10. Note that the sensible heat flux is not shown because of its negligible contribution. Under climate warming, during the developing of ENSO, the eastern equatorial Pacific is characterized by a heat loss to the atmosphere, which comes mainly from a reduction of both latent heat flux and shortwave radiation. Under climate cooling, the heat gain in the eastern equatorial ocean from the atmosphere is resulted from an increase in the latent heat flux, while the change in the shortwave radiation plays a minor role. Over the eastern equatorial Pacific (west of 120°W), the cooling effect by the shortwave radiation is resulted from an increase of the low-level cloud in both WMS and CLS (not shown). In both cases, in addition, the longwave radiation acts to slightly warm the eastern equatorial ocean.

Since the latent heat flux is dominant among the four components in the surface heat flux, we further decompose
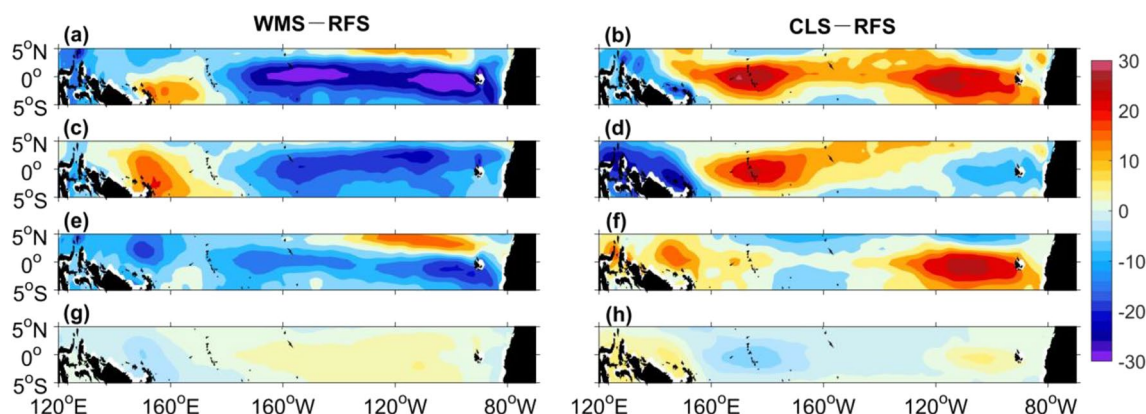


**Fig. 10** Changes in **a, b** total air-sea surface heat flux and its components (W m$^{-2}$) of **c, d** shortwave radiation, **e, f** latent heat flux, and **g, h** longwave radiation from RFS to WMS (left) and from RFS to CLS (right) during the developing phase of ENSO. Positive indicates flux into the ocean from the atmosphere. The sensible heat flux is not shown because of its small magnitude

it into the following four major terms (e.g., Richter and Xie 2008; Luo et al. 2017):

$$Q_e' = Q_{eo} + Q_{ew} + Q_{erh} + Q_{edt}$$
$$= \frac{\partial Q_e}{\partial T}T' + \frac{\partial Q_e}{\partial W}W' + \frac{\partial Q_e}{\partial RH}RH' + \frac{\partial Q_e}{\partial \Delta T}\Delta T' \quad (6)$$

where prime denotes the difference of WMS or CLS from RFS. The four components represent the Newtonian cooling ($Q_{eo}$), the effects of wind-evaporation-SST (WES) interaction ($Q_{ew}$) (Xie and Philander 1994), the effects of relative humidity ($Q_{erh}$), and air-sea surface temperature difference ($Q_{edt}$), respectively. As shown in Fig. 11, while the cooling effect of the latent heat flux in WMS is dominated by Newtonian cooling, its warming effect in CLS is by both Newtonian cooling and the effects of relative humidity. The increasing $Q_{erh}$ in CLS is due to a significant increase of the relative humility during the developing of ENSO compared to that in RFS. In both WMS and CLS, the feedbacks of WES and air-sea surface temperature difference appear to contribute negatively to the change in the latent heat flux.

## 5 Changes in Bjerknes linear stability index

Our above heat budget analysis has identified four linear dynamic terms that are important in the enhanced (reduced) ENSO amplitude in WMS (CLS), i.e., the ZA, MA, TH, and EK terms. On the other hand, the surface heat flux response (i.e., the TD term) always acts to damp the ENSO amplitude
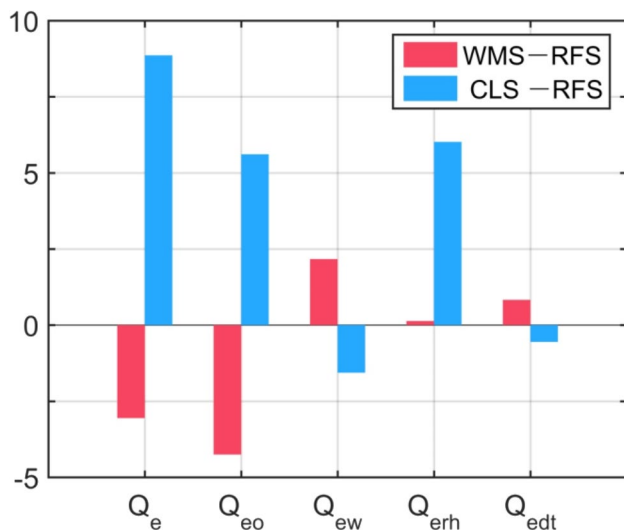
change. To quantitatively evaluate the overall ENSO stability in RFS, WMS and CLS, we adopt the BJ index introduced by Jin et al. (2006). A detailed description about the BJ index is presented in "Appendix B". As a measure of overall linear ENSO growth rate essentially related to ENSO amplitude, the BJ index has been found to be a useful tool for a comprehensive and quantitative analysis of relative contributions of positive feedback effect and damping process effect (e.g., Kim et al. 2014; An and Bong 2016; Chen et al. 2016). Following Jin et al. (2006), the positive effect refers to the ZA, TH, and EK feedbacks, and the damping effect includes the dynamic damping due to effect of mean advection (MD) and the thermodynamic damping (TD) related to the surface heat flux associated with ENSO variability. It should be noted that the MD effect here is composed largely of the MA feedback discussed above in Sect. 4.3.

Figure 12 illustrates these feedback and process effects as well as their sum BJ index for the three cases. It is found that, among the three positive feedbacks, the EK feedback appears to be one order smaller than the ZA or TH feedback. Compared to these in RFS, in addition, all the positive feedbacks are intensified in WMS but weakened in CLS, which is consistent with our heat budget analysis results presented above in Sect. 4. The most significant change is the ZA, with its intensity being increased by 0.21 from 0.84 year$^{-1}$ in RFS to 1.05 year$^{-1}$ in WMS and being decreased by 0.13–0.71 year$^{-1}$ in CLS. Regarding the damping processes, the MD is found to increase in WMS but decrease in CLS. The TD, however, has the opposite changes, i.e., it is decreased in WMS but increased in CLS.

When adding up all the positive feedbacks and damping processes, it can be seen in Fig. 12 that the BJ index is increased by 0.12 from 0.27 year$^{-1}$ in RFS to 0.39 year$^{-1}$
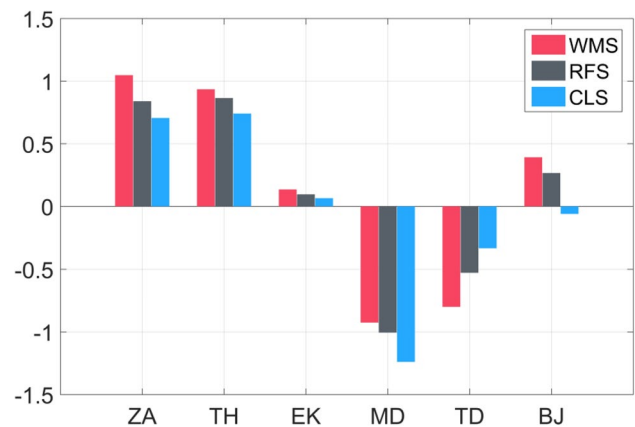


**Fig. 11** Changes in latent heat flux $Q_e$ and its four major components (W m$^{-2}$) including Newtonian cooling effect $Q_{eo}$, WES effect $Q_{ew}$, relative humidity effect $Q_{erh}$, and stability effect $Q_{edt}$ during the developing phase of ENSO in the Niño3 region from RFS to WMS (red bars) and from RFS to CLS (blue bars)



**Fig. 12** The BJ index and its components (year$^{-1}$) in RFS (black), WMS (red), and CLS (blue). ZA, TH, EK, MD, TD, and BJ represent zonal advective feedback, thermocline feedback, Ekman feedback, dynamic damping, thermodynamic damping, and BJ index (a sum of previous five terms), respectively

in WMS but is decreased by 0.33 to $-0.06$ year$^{-1}$ in CLS. Therefore, this comprehensive and quantitative analysis indicates that climate warming (cooling) induces a larger (smaller) BJ index and thus an increased (decreased) ENSO amplitude, lending further support to the conclusions from our previous analysis based upon the mixed layer heat budgets.

# 6 Summary

In this study, we have examined the response of the ENSO amplitude to climate warming and cooling in NCAR's CESM. Results show that warming the ocean surface induces an increase of the ENSO amplitude and cooling decreases the ENSO amplitude, and these changes are statistically significant. The mixed layer heat budget analysis applied over the eastern equatorial Pacific identified four dynamical processes responsible for the opposite changes of the ENSO tendency, in the order of importance, they are the ZA, MA, TH, and EK feedbacks. Taking El Niño as an example, schematic diagrams are shown in Fig. 13 to demonstrate the equatorial dynamical processes during its developing phase in RFS and their changes in WMS. Under climate warming, a wind anomaly of the same magnitude across the equatorial Pacific will induce a stronger zonal current change in the eastern equator (a stronger ZA feedback), which in turn will result in a greater weakening of upwelling (a stronger EK feedback) and thus a larger



**Fig. 13** Schematics of the equatorial dynamical processes during the developing phase of an El Niño in **a** RFS, and **b** WMS. The big black arrows represent anomalous zonal wind stress. The small arrows indicate anomalous currents in zonal, meridional, and vertical directions, with black for RFS and red for WMS. Color shading represents the SSTA. The black solid and dashed lines denote the thermocline depth and its change, respectively

thermocline change (a stronger TH feedback). In response to the climate warming, in addition, a slowdown of the STC will give rise to a narrower meridional width of SSTA around the equator, leading to a stronger MA feedback. The opposite is true for the case of climate cooling.

The TD term appears to be the major damping term for the SST changes in response to both warming and cooling. In the warming climate, the surface heat loss to the atmosphere is mainly due to a reduction of both shortwave radiation and latent heat flux, with the latter being dominated by Newtonian cooling. In the cooling climate, the surface heat gain from the atmosphere is originated from an increase in the latent heat flux, which in turn is due to the change of Newtonian cooling and the effect of relative humidity.

The BJ index, an overall measurement of the linear effects on the ENSO growth rate, is found to be increased in WMS but decreased in CLS, which is resulted from the positive contributions of changes in the ZA, TH, EK and MD effects in both cases. This result supports that BJ index can be a useful tool for assessing the instability of ENSO when the climate mean state changes.

The dynamic perturbations essential for the ENSO amplitude change (Fig. 5) are closely connected to the changes in the climatological mean states, which have also experienced remarkable changes in response to climate warming and cooling. For instance, the Pacific STC slows down under climate warming but spins up under climate cooling. The warming induces an El Niño-like SST warming pattern and westerly wind anomalies, and the cooling produces the maximum SSTA in the central equator and easterly wind anomalies (Liu et al. 2017a). In addition, in contrast to more stratified upper ocean due to greater warming at the surface in WMS, the upper ocean is less stratified and the thermocline appears to be deeper in CLS. All these above changes will have an indispensable influence on the tropical SST pattern and subsurface temperature structure, and thus on the dynamic and thermodynamic feedbacks/processes responsible for the ENSO amplitude changes.

# Appendix A: meridional volume transport

The associated change in the meridional volume transport across the tropical ocean is largely determined by the wind-stress driven Ekman transport. Following McPhaden and Zhang (2002), the meridional Ekman transport per unit longitude is calculated by the equation:
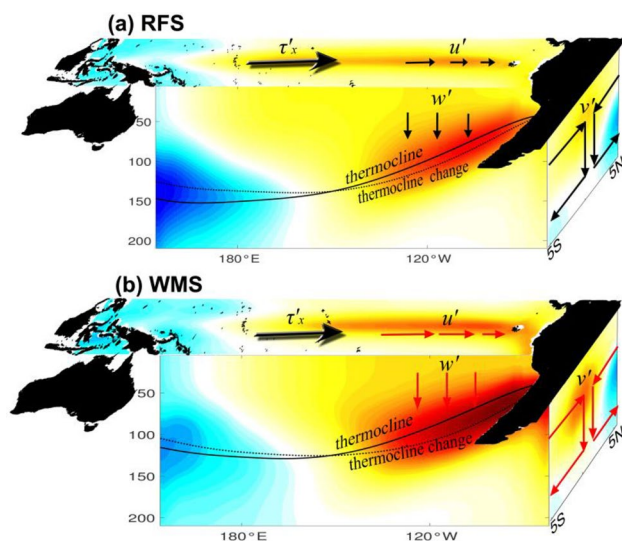
$$M_E = -\tau_x/\rho_0 f \tag{7}$$

where $\tau_x$ is the zonal wind stress, and $f$ is the Coriolis parameter. The transports are confined approximately to the upper 50 m in the tropical oceans (Ralph and Niiler 1999). The Ekman transport divergence between 9°N and 9°S can be estimated as:

$$M_1 = \int_A^B M_E[9°N] - \int_C^D M_E[9°S] \tag{8}$$

where A and B give the longitudinal range along 9°N (between 126°E and 83°W) and C and D the range along 9°S (between 148°E and 78°W), respectively. The net surface layer divergence is obtained by Ekman transports minus the opposing surface layer geostrophic transports, which is obtained from an integration of geostrophic velocity over the upper 50 m. The water depth of 900 m is used as the reference level for geostrophic calculations.

The calculation of the STC transport for the interior ocean across 9°N and 9°S follows Luo et al. (2009). The interior transport is the sum of the equatorial geostrophic transport integrated from 140°E to 83°W in 9°N and from 160°E to 78°W in 9°S. The mixed layer depth (0.125 kg m$^{-3}$ criterion) is considered as the upper boundary for the calculation of interior transport when it is denser than the top layer of the STC. For RFS, the top and bottom of the STC layer are marked by 22.0 and 26.0 kg m$^{-3}$ isopycnals at 9°N, and by 22.5 and 26.2 kg m$^{-3}$ isopycnals at 9°S, respectively. Because the mean state is changed significantly under both warming and cooling scenarios, the density classes defined are generally 21.5 kg m$^{-3}$ < $\sigma_0$ < 25.5 kg m$^{-3}$ at 9°N and 22.0 kg m$^{-3}$ < $\sigma_0$ < 25.7 kg m$^{-3}$ at 9°S for WMS, and 22.5 kg m$^{-3}$ < $\sigma_0$ < 26.5 kg m$^{-3}$ at 9°N and 23.0 kg m$^{-3}$ < $\sigma_0$ < 26.7 kg m$^{-3}$ at 9°S for CLS.

## Appendix B: Bjerknes linear stability index

Based on the recharge oscillator framework and with a number of assumptions for simplifications in the mixed layer heat budget equation (Jin et al. 2006; Kim and Jin 2011), the SST tendency over the eastern equatorial Pacific can be estimated as follows:

$$\frac{d\langle T\rangle_E}{dt} = R\langle T\rangle_E + F\langle h\rangle_W \tag{9}$$

where $\langle\cdot\rangle_E$ and $\langle\cdot\rangle_W$ represent the eastern and western boxed averaged quantity, respectively. With the latitudinal range from 5°N and 5°S, the two boxes are separated based on a nodal line by computing the empirical orthogonal function of detrended SSTA over the tropical Pacific and then regressing ocean heat content anomalies onto the first principal component. Specifically, for this study the nodal line separating the eastern and western boxes is chosen to be 174°W in RFS, 161°W in WMS and 179°E in CLS, respectively. $T$ is the SSTA, $h$ is the thermocline depth, and $F$ is the frequency factor of interannual oscillator. $R$ is the growth rate of the ENSO oscillator, in this study, we will examine the growth rate measured by the BJ index. $R$ can be expressed by:

$$R = -\left[a_1\frac{\langle\Delta\bar{u}\rangle_E}{L_x} + a_2\frac{\langle\Delta\bar{v}\rangle_E}{L_y}\right] - \alpha_s + \mu_a\beta_u\left\langle-\frac{\partial\bar{T}}{\partial x}\right\rangle_E$$
$$+ \mu_a\beta_h\left\langle\frac{\bar{w}}{H_1}\right\rangle_E \alpha_h + \mu_a\beta_w\left\langle-\frac{\partial\bar{T}}{\partial z}\right\rangle_E \tag{10}$$

where the $\bar{u}$, $\bar{v}$, $\bar{w}$ and $\bar{T}$ are climatological currents and temperature, respectively; $H_1$ represents the mixed layer depth; $L_x$ and $L_y$ represent the longitudinal and latitudinal lengths of the eastern box, respectively; $a_1$ and $a_2$ are estimated using SSTA averaged zonally or meridionally at boundaries and averaged SSTA over the box; $\alpha_s$, $\mu_a$, $\beta_h$, $\beta_w$, $\beta_u$, and $\alpha_h$ reflect atmospheric dynamic sensitivities to ENSO SST forcing as well as the ocean dynamic sensitivities to ENSO wind forcing. Using the least-squares regression method (Jin et al. 2006; An and Bong 2016), these coefficients are computed from approximated balance equations, i.e., $\langle Q\rangle_E = -\alpha_s\langle T\rangle_E$, $[\tau_x] = \mu_a\langle T\rangle_E$, $\langle h\rangle_E - \langle h\rangle_W = \beta_h[\tau_x]$, $\langle H(\bar{w})w\rangle_E = -\beta_w[\tau_x]$, $\langle u\rangle_E = \beta_u[\tau_x] + \beta_{uh}\langle h\rangle_W$, and $\langle H(\bar{w})T_{sub}\rangle_E = \alpha_h\langle h\rangle_E$, where $Q$ is the net downward heat flux, $[\tau_x]$ is the equatorial trade wind anomaly, $H(\bar{w})$ is a step function to consider only climatological upwelling, and $\beta_{uh}$ refers to geostrophic current adjusted to thermocline.

On the right hand side of Eq. (10), in an order of left to right, the first two negative terms represent the dynamic damping, the third negative term represents the thermodynamic damping, and the next three positive terms represent the effects of the zonal advective feedback, thermocline feedback, and Ekman feedback, respectively.

## References

Alory G, Meyers G (2009) Warming of the upper equatorial Indian Ocean and changes in the heat budget (1960–99). J Clim 22:93–113. https://doi.org/10.1175/2008JCLI2330.1

An S-I, Bong H (2016) Inter-decadal change in El Niño-Southern Oscillation examined with Bjerknes stability index analysis. Clim Dyn 47:967–979. https://doi.org/10.1007/s00382-015-2883-8

Bellenger H, Guilyardi E, Leloup J, Lengaigne M, Vialard J (2014) ENSO representation in climate models: from CMIP3 to CMIP5. Clim Dyn 42:1999–2018. https://doi.org/10.1007/s00382-013-1783-z

Bulić IH, Branković Č, Kucharski F (2012) Winter ENSO teleconnections in a warmer climate. Clim Dyn 38:1593–1613. https://doi.org/10.1007/s00382-010-0987-8

Cai W, Borlace S, Lengaigne M et al (2014) Increasing frequency of extreme El Niño events due to greenhouse warming. Nat Clim Chang 5:1–6. https://doi.org/10.1038/nclimate2100

Cai W, Wang G, Santoso A et al (2015) Increased frequency of extreme La Niña events under greenhouse warming. Nat Clim Chang 5:132–137. https://doi.org/10.1038/nclimate2492

Capotondi A, Wittenberg A, Masina S (2006) Spatial and temporal structure of Tropical Pacific interannual variability in 20th century coupled simulations. Ocean Model 15:274–298. https://doi.org/10.1016/j.ocemod.2006.02.004

Chen L, Li T, Yu Y (2015) Causes of strengthening and weakening of ENSO amplitude under global warming in four CMIP5 Models*. J Clim 28:3250–3274. https://doi.org/10.1175/jcli-d-14-00439.1

Chen L, Yu Y, Zheng W (2016) Improved ENSO simulation from climate system model FGOALS-g1.0 to FGOALS-g2. Clim Dyn 47:2617–2634. https://doi.org/10.1007/s00382-016-2988-8

Chen L, Li T, Yu Y, Behera SK (2017) A possible explanation for the divergent projection of ENSO amplitude change under global warming. Clim Dyn 0:0. https://doi.org/10.1007/s00382-0

Cowan T, Cai W, Ng B, England M (2015) The response of the Indian Ocean dipole asymmetry to anthropogenic aerosols and greenhouse gases. J Clim 28:2564–2583. https://doi.org/10.1175/JCLI-D-14-00661.1

DiNezio PN, Clement AC, Vecchi G et al (2009) Climate response of the equatorial pacific to global warming. J Clim 22:4873–4892. https://doi.org/10.1175/2009JCLI2982.1

Dinezio PN, Kirtman BP, Clement AC et al (2012) Mean climate controls on the simulated response of ENSO to increasing greenhouse gases. J Clim 25:7399–7420. https://doi.org/10.1175/JCLI-D-11-00494.117-3544-x

Dong L, Zhou T, Wu B (2014) Indian Ocean warming during 1958–2004 simulated by a climate system model and its mechanism. Clim Dyn 42:203–217. https://doi.org/10.1007/s00382-013-1722-z

Horel JD, Wallace JM (1981) Planetary-scale phenomena associated with the Southern Oscillation. Mon Weather Rev 109:813–829

Jin F-F, Kim ST, Bejarano L (2006) A coupled-stability index for ENSO. Geophys Res Lett 33:L23708. https://doi.org/10.1029/2006GL027221

Kim ST, Jin F-F (2011) An ENSO stability analysis. Part II: results from the twentieth and twenty-first century simulations of the CMIP3 models. Clim Dyn 36:1609–1627. https://doi.org/10.1007/s00382-010-0872-5

Kim ST, Cai W, Jin F-F, Yu J-Y (2014) ENSO stability in coupled climate models and its association with mean state. Clim Dyn 42:3313–3321. https://doi.org/10.1007/s00382-013-1833-6

Li Z, Luo Y (2018) Response of the tropical Indian Ocean to greenhouse gases versus aerosol forcing in the GFDL CM3 coupled climate model. Atmos Ocean. https://doi.org/10.1080/07055900.2018.1427040

Li G, Xie S-P, Du Y, Luo Y (2016) Effects of excessive equatorial cold tongue bias on the projections of tropical Pacific climate change. Part I: the warming pattern in CMIP5 multi-model ensemble. Clim Dyn 47:3817–3831. https://doi.org/10.1007/s00382-016-3043-5

Li G, Xie S-P, He C, Chen Z (2017) Western Pacific emergent constraint lowers projected increase in Indian summer monsoon rainfall. Nat Clim Chang 7:708–712. https://doi.org/10.1038/nclimate3387

Liu L, Yu W, Li T (2011) Dynamic and thermodynamic air-sea coupling associated with the Indian Ocean Dipole diagnosed from 23 WCRP CMIP3 models. J Clim 24:4941–4958. https://doi.org/10.1175/2011JCLI4041.1

Liu F, Luo Y, Lu J et al (2017a) Asymmetric response of the equatorial Pacific SST to climate warming and cooling. J Clim 30:7255–7270. https://doi.org/10.1175/JCLI-D-17-0011.1

Liu F, Luo Y, Lu J, Wan X (2017b) Response of the tropical Pacific Ocean to El Niño versus global warming. Clim Dyn 48:935–956. https://doi.org/10.1007/s00382-016-3119-2

Luo Y, Rothstein LM, Zhang R-H (2009) Response of Pacific sub-tropical-tropical thermocline water pathways and transports to global warming. Geophys Res Lett 36:L04601. https://doi.org/10.1029/2008GL036705

Luo Y, Lu J, Liu F, Garuba O (2017) The role of ocean dynamical thermostat in delaying the El Niño-like response over the equatorial Pacific to climate warming. J Clim 30:2811–2827. https://doi.org/10.1175/JCLI-D-16-0454.1

McPhaden MJ, Zhang D (2002) Slowdown of the meridional overturning circulation in the upper Pacific Ocean. Nature 415:603–608. https://doi.org/10.1038/415603a

McPhaden MJ, Zebiak SE, Glantz MH (2006) ENSO as an integrating concept in earth science. Science 314:1740–1745. https://doi.org/10.1126/science.1132588

Merryfield WJ (2006) Changes to ENSO under CO2 doubling in a multimodel ensemble. J Clim 19:4009–4027. https://doi.org/10.1175/JCLI3834.1

Philander SG (1990) El Niño, La Niña, and the Southern Oscillation. Academic Press, London

Philip S, van Oldenborgh GJ (2006) Shifts in ENSO coupling processes under global warming. Geophys Res Lett 33:L11704. https://doi.org/10.1029/2006GL026196

Ralph EA, Niiler PP (1999) Wind-driven currents in the tropical Pacific. J Phys Oceanogr 29:2121–2129

Richter I, Xie S-P (2008) Muted precipitation increase in global warming simulations: a surface evaporation perspective. J Geophys Res 113:D24118. https://doi.org/10.1029/2008JD010561

Stevenson SL (2013) Significant changes to ENSO strength and impacts in the twenty-first century: results from CMIP5. Geophys Res Lett 39:L17703. https://doi.org/10.1029/2012GL052759

Su J, Zhang R, Li T et al (2010) Causes of the El Niño and La Niña amplitude asymmetry in the equatorial eastern Pacific. J Clim 23:605–617. https://doi.org/10.1175/2009JCLI2894.1

Tsonis AA, Hunt AG, Elsner JB (2003) On the relation between ENSO and global climate change. Meteorol Atmos Phys 84:229–242. https://doi.org/10.1007/s00703-003-0001-7

van Oldenborgh GJ, Philip SY, Collins M (2005) El Niño in a changing climate: a multi-model study. Ocean Sci 1:81–95. https://doi.org/10.5194/os-1-81-2005

Watanabe M, Kug J-S, Jin F-F et al (2012) Uncertainty in the ENSO amplitude change from the past to the future. Geophys Res Lett 39:L20703. https://doi.org/10.1029/2012GL053305

Xie S-P, Philander SG (1994) A coupled ocean–atmosphere model of relevance to the ITCZ in the eastern Pacific. Tellus A 46:340–350. https://doi.org/10.1034/j.1600-0870.1994.t01-1-00001.x

Xie S-P, Lu B, Xiang B (2013) Similar spatial patterns of climate responses to aerosol and greenhouse gas changes. Nat Geosci 6:828–832. https://doi.org/10.1038/NGEO1931

Yeh S-W, Kirtman BP (2007) ENSO amplitude changes due to climate change projections in different coupled models. J Clim 20:203–217. https://doi.org/10.1175/JCLI4001.1

Zhang W, Jin F-F, Zhao J-X, Li J (2013) On the bias in simulated ENSO SSTA meridional widths of CMIP3 models. J Clim 26:3173–3186. https://doi.org/10.1175/JCLI-D-12-00347.1

Zheng X-T, Xie S-P, Lv L-H, Zhou Z-Q (2016) Intermodel uncertainty in ENSO amplitude change tied to Pacific Ocean warming pattern. J Clim 29:7265–7279. https://doi.org/10.1175/JCLI-D-16-0039.1

Zhou Z-Q, Xie S-P, Zheng X-T et al (2014) Global warming-induced changes in El Niño teleconnections over the North Pacific and North America. J Clim 27:9050–9064. https://doi.org/10.1175/JCLI-D-14-00254.1